RSC Advances

PAPER

View Article Online
View Journal | View Issue

Cite this: *RSC Adv.*, 2026, **16**, 22488

Interfacing a nanostructured nickel oxide layer displaying fractal-like features with graphene: chemiresistive behaviour and GFET implementation

Michele Zanotti, [a] Elena Rolfi,†[a] Sonia Freddi, [ab] Stefania Pagliara, [a] Vincent Mazzola,[c] Filiberto Ricciardella, ‡[c] Leandro Sacco [c] and Luigi Sangaletti *[a]

An interface between graphene and a nanostructured nickel oxide (NiO) layer with fractal-like features was prepared by spark ablation coupled with impaction printing at 0.2 mbar. The chemiresistive behavior of the interface was investigated by exposing the surface to ammonia (NH_3) and nitrogen dioxide (NO_2). Results showed that the NiO layer made the overall system more selective towards NH_3, indicating that the p-type character of the graphene layer was strengthened by the oxide deposition, which was consistent with the results of microRaman spectroscopy. With respect to the pristine graphene layer, the response to NO_2 decreased by a factor of approximately 2 over the NO_2 concentration range from 2 to 6 ppm, while we observed a 3-fold increase in the response to NH_3 over a concentration range of 10 to 40 ppm. The graphene layer covered with NiO, showing the highest response to NH_3, was selected to fabricate a graphene-based field effect transistor to be operated as a gas sensor and to eventually investigate the effect of NH_3 on carrier mobility. The NH_3 sensing based on tracing the Dirac point shift was demonstrated. Compared with the resistivity variation measured in the chemiresistive configuration, when the change in the Dirac point was traced, the calibration curves showed a three-fold increase in the sensitivity towards NH_3. These findings further show the enhancement of the sensing properties of graphene due to the incorporation of nanostructured, fractal-like NiO layer.

Received 2nd September 2025
Accepted 11th April 2026

DOI: 10.1039/d5ra06573a

rsc.li/rsc-advances

1 Introduction

Graphene-based field effect transistors (GFETs) constitute a unique platform for sensing and, in general, for the investigation of transport properties in two-dimensional (2D) systems. Functionalization represents one of the key features to steer the transport properties of graphene (Gr) layers. Functionalization can be achieved through a manifold of strategies, which include decoration with metallic or oxide nanoparticles (NPs), molecular layer deposition with covalent (*e.g.* grafting) or van der Waals (*e.g.*, phthalocyanine) interactions, and fabrication of heterostructure systems.[1–5] In the field of gas sensing, functionalization is aimed at increasing the sensitivity and/or the selectivity of sensing devices.[6–10] Chemiresistors and GFETs represent the most used sensing transduction devices based on the transport properties of graphene layers. The usual GFET-based gas sensing mechanism relies on the high sensitivity of graphene to the presence of gas molecules, which affects the conductivity of graphene-based transistor channels.[11–22] As such, GFET-based gas sensors offer real-time monitoring of gas concentrations and are suitable for various applications, including environmental monitoring, industrial safety, and healthcare.[23] GFET-based gas sensors offer several advantages, including exceptional sensitivity—potentially down to the single-molecule level[12]—fast response of the sensing layer,[24] and strong potential for miniaturization, which make them well suited for portable and wearable gas sensors. Graphene-based chemiresistors can be regarded as GFETs in which the gate voltage has been set to zero. When a gate voltage is applied, it is possible to track the source–drain current and therefore explore the sensor response as a function of gas exposure conditions. The transition point where the majority charge carriers shift from holes to electrons is known as the charge neutrality point, often referred to as the Dirac point. It occurs when the electron and hole densities are nearly equal, and the graphene conductance reaches its minimum.[25] Furthermore, by tuning the gate voltage, as it usually occurs in GFETs, further doping of the

[a]*Department of Mathematics and Physics, Università Cattolica del Sacro Cuore, Via della Garzetta, 48 25133 Brescia, Italy. E-mail: luigi.sangaletti@unicatt.it*

[b]*Institute of Photonics and Nanotechnologies – Consiglio Nazionale delle Ricerche (IFN-CNR), LNESS Laboratory, Via Anzani 42, 22100 Como, Italy*

[c]*VSParticle, Oostsingel 209, 2612HL Delft, The Netherlands*

† Present address: Department of Physics, Politecnico di Milano, P. le Leonardo da Vinci 32, 20131 Milan, Italy.

‡ Present affiliation: Quantum Technology Department, High Tech Industry, TNO, Stieltjesweg 1, 2628CK Delft, The Netherlands.

graphene channel can be realized to enhance the selectivity towards specific target gas molecules.

In this study, a novel interface between graphene and a nanostructured, fractal-like, nickel oxide (NiO) layer was prepared, adopting a fully dry printing process based on spark ablation under ambient conditions. The spark ablation technique is a clean and versatile method for producing highly pure NPs in an aerosol originating from bulk conductive or properly doped semiconductive electrodes.[26] The aerosol containing the NPs can be deposited by inertial impaction on any substrate, accelerating the aerosol through a nozzle by means of a pressure difference between the spark ablation generator and chamber at a low pressure where the target substrate is located. Single-step and highly precise printing is enabled by moving the stage and the monolithically attached target substrate in the *XYZ* direction. As such, the spark ablation approach coupled with a single-step dry printing system enables to deposit the sensing layer at the very last step of the sensor's fabrication process,[27] avoiding (1) any lithographic and etching steps for structuring the gas sensitive nanomaterials, (2) interferences with other contaminants, such as photoresist, and (3) the exposure of the sensing layers to post-treatments, such as etching or curing.

The use of nanostructured metal oxides (MOx), including NiO, in combination with graphene or reduced-graphene oxide (r-GO) is well known in the case of blends at the nanoscale or in the case of r-GO decoration with nanoparticles.[28–40] However, the use of MOx layers grown on top of graphene for gas sensing is far less explored.[41,42] On the other hand, NiO is itself used as a nanostructured MOx for gas sensing applications.[43,44] Therefore, the combination of a nanostructured NiO layer on top of the Gr layer provides a unique opportunity to explore the capability of the NiO layer to boost the sensing properties of graphene, providing, in principle, a pathway to steer the selectivity.

Most of the literature so far[28–44] deals with rGO–NiO nanoparticle composites. With spark ablation, we do not produce composites but NiO/Gr heterostructures, namely a NiO layer on top of a single, cm-sized, graphene layer. This leads to better control at the interface between NiO and Gr, which is extended over all the graphene surface, rather than being a random arrangement of Gr flakes intermixed or decorated with NiO nanostructures. We believe that our choice provides a clear 2D architecture with the stacking of the two layers, which is particularly suitable for the GFET driving of the sensing capabilities.

Moreover, we utilized a nanostructured NiO layer because its porous, fractal-like structure offers a large surface-to-volume ratio, enhancing sensing performance. This layer covers the graphene without blocking gas access to the interface, enabling the graphene to act also as an efficient transport layer for the signal.

The present sensing devices are investigated by exposing them to both ammonia (NH_3) and nitrogen oxide (NO_2). These two analytes are often considered as test gases for novel carbon-based sensing systems because they are expected to provide opposite effects on the chemiresistive properties, *i.e.*, NO_2 and NH_3 are considered oxidizing and reducing gases, respectively.[12] In particular, in the present study, we consider NH_3 sensing using both chemiresistive and GFET readout configurations. We focus on NH_3 as it is a target gas of relevance for several applications in the sensing field, such as environmental control, healthcare, and food and beverage quality assessment.[45–49]

The results show that the NiO coverage makes the transducer more selective to NH_3, indicating that the p-type character of the layer is strengthened by the oxide deposition. This is consistent with the results of the microRaman spectroscopy characterization of the sensing layers. With the sample that displayed the highest response to NH_3, a GFET was prepared in order to investigate the effect of NH_3 on carrier mobility. NH_3 sensing based on the tracking of the Dirac point shift in the GFET is demonstrated, which appears as an effective way to further increase the sensitivity to a specific analyte with respect to the simple chemiresistive readout.

2 Experimental

2.1 Graphene layer and deposition of NiO NPs

Graphene layers were purchased from Graphenea. Each sample consisted of a stack of p-type silicon/silicon nitride (Si_3N_4) as a dielectric/graphene layer. The stacking of layers is shown in Fig. 1a and b.

A spark-ablation-coupled printing-impaction system was used to decorate the graphene layers with Ni NPs. The deposition was performed using a VSP-P1 nanoprinter (VSParticle B.V, Fig. 1c and d). The nanoprinter contained a VSP-G1 (VSParticle B.V) NP generator equipped with two Ni electrodes having high purity (99.9%). Applying a potential of 1 kV and a current of 5 mA between the two electrodes facing each other, sparks were generated under ambient conditions. Argon was used as a carrier gas with a flow rate of 1 L min^{-1} during the spark ablation process. The generated aerosol containing NPs was flown towards the nanoprinter. The samples were placed into a chamber kept at RT and 0.15–0.20 mbar. The pressure difference between the NP generator and the chamber resulted in the jet impaction of the NP aerosol onto the graphene surface. A programmable serpentine pattern was designed with variable pitches and printing speed in view of having different coverage of the graphene layers. The printing was enabled by moving the stage in XY directions while keeping the nozzle-to-substrate distance equal to 200 μm. The printing speed ranged from 200 μm s^{-1} to 500 μm s^{-1}, as reported in Table 1. Based on the nanoprinter calibration carried out with the parameters specified above and on the pitch size, the thickness for the printed layers ranges from 0.80 μm to 1.92 μm, as detailed in Table 1.

2.2 Characterization techniques

2.2.1 Surface imaging and microRaman spectroscopy. Field-emission scanning electron microscopy (FE-SEM) images were acquired with Hitachi Regulus 8230, with an accelerating voltage of 3 kV, using the upper detector. Optical images were collected with the Leica optical microscope of the microRaman

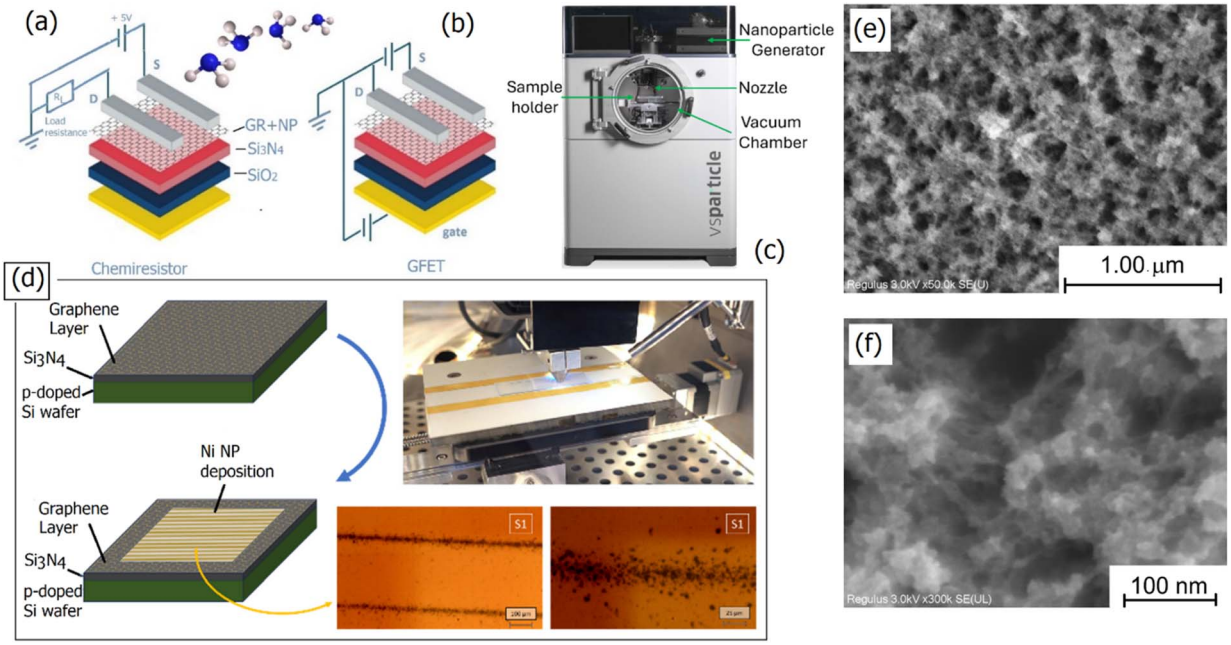

Fig. 1 Schematic of the electrical wiring used for the chemiresistor (a) and GFET (b) measurements. Overall view of the NP deposition system (c). Deposition raster scheme, printing stage inside the vacuum-tight deposition chamber, and optical microscopic images (d). SEM planar-view images of the NiO/graphene surface collected at 50 000× (e) and 300 000× (f).

Table 1 Samples covered with Ni NPs and corresponding deposition parameters

Sample	Print speed (µm s^{-1})	Area (µm^2)	Pitch (µm)	Estimated thickness (µm)	Substrate
Pristine graphene	—	8000 × 8000	—	—	Si_3N_4
S1	400	8000 × 8000	300	0.80	Graphene on Si_3N_4
S2	300	8000 × 8000	300	1.07	Graphene on Si_3N_4
S3	200	8000 × 8000	300	1.60	Graphene on Si_3N_4
S4	500	8000 × 8000	50	1.92	Graphene on Si_3N_4

spectrometer. Raman spectra were collected with a Renishaw microRaman spectrometer equipped with an 1800 L mm^{-1} grating and a He–Ne laser, with a power equal to 5 mW at the sample. The laser beam was focused with a 100× microscope objective.

2.2.2 XPS spectroscopy. X-ray photo-electron spectroscopy (XPS) data were collected under ultra-high vacuum conditions (base pressure = 3×10^{-10} mbar) with a properly calibrated[50] Scienta R3000 electron analyzer and the Al Kα line of a twin anode X-ray source. The overall energy resolution of the XPS probe was set at 0.9 eV.

2.2.3 GFET and chemiresistor measurements. Chemiresistive measurements were carried out by collecting dynamical response curves during repeated exposures to NH_3 in ambient air with 50% relative humidity (R.H.) and NO_2 in a sealed chamber with R.H. = 4%. The chemiresistor wiring scheme is sketched in Fig. 1a. The samples were mounted on a custom-made printed circuit board. The gate contact (G) is underneath the silicon substrate. The source (S) and drain (D) contacts are made of silver paint, and two metal pins are placed on top of them to anchor the sample and grant stable contacts. For chemiresistive measurements, only the S and D contacts were used. In this case, a 5 V fixed voltage between S and ground was applied, and a load resistance R_L was added to limit the current through the S–D channel and avoid overheating. The resistance change upon gas exposure (R_{sensor}) was evaluated through a measure of the voltage drop across the S–D channel, according to the following equation:

$$R_{sensor} = V_{SD} \times R_L/(5 - V_{SD})$$

Data were collected with a NI board controlled through LabView. For the GFET measurements (Fig. 1b), a Keithley nanoamperometer (model 2634B) was used. The control of the device and the automated data acquisition were enabled using a Python script developed for this purpose using the PyLab library. A voltage drop between the source and drain terminals was maintained at a constant value of 1.1 V. Meanwhile, the gate voltage was systematically varied from 0 V to 60 V with steps of 1 V. At each step of the gate voltage, the current passing through the source–drain terminals was averaged over a duration of 0.5 seconds, with a sampling rate of 200 Hz.

3 Results and discussion

3.1 Surface imaging

Optical and SEM microscopy imaging was carried out to characterize the morphology of the samples at different scale lengths. Fig. 1d shows the scheme of the sample preparation, along with the deposition equipment and the optical images of the deposition paths. Additional optical images of the four samples are shown and analysed in Fig. S1 and S2 (top panel) of the SI file, while the typical cross-sectional view of single printed lines is shown in the bottom panel of Fig. S2.

The deposition of the nanostructured layers could be tuned by steering the deposition parameter set, which included NP flux, nozzle-to-sample distance, linear speed of the nozzle, and pitch, which is the distance between two subsequent printed lines. In the dataset of the samples investigated here, the nozzle-to-surface distance and the NP flux were constant, while both speed and pitch were changed as detailed in Table 1. Based on the analysis of the optical images (Fig. S1), we could conclude that the most uniformly covered surface was that of sample S4. The amount of NP increased from sample S1 to S3. Samples S1 and S2 showed tiny NP tracks separated by 300 μm (dark lines in Fig. S1), while, as the nozzle speed was decreased, the side regions of NP appeared along the tracks (Fig. S1 and S2). These regions became visible in sample S3, though they still were too separated from one another to provide the full coverage of the surface, which was achieved in sample S4 by reducing the pitch from 300 μm to 50 μm. In this sample, the thickness of a single line was the smallest in the dataset, due to the highest printing speed (500 μm s^{-1}), but the overlap among neighbouring lines made the overall thickness the largest in the set.

Representative SEM images of the NP layer are shown in Fig. 1e and f. A large part of the surface of the sample was covered by a layer that appeared highly porous, with irregular patterns. Many fractal materials (*e.g.* aerogels, carbon nanomaterials, some oxides, soot, and biological structures) exhibit these porous sponge-like networks. For this reason, we looked for possible fractal-like properties in our samples. Indeed, as detailed in the SI file, a fractal dimension analysis was carried out on 8 different FE-SEM images collected at different magnifications (25k, 50k, 150k, 300k) from two different points of the surface (Fig. S6 of the SI file).

For the estimation of self-similarity properties, the box-counting fractal dimension, the mean lacunarity, the mean perimeter–area exponent, and the power spectral density analysis methods were considered.

The box-counting method overlays grids of varying sizes (ε) on a 2D image and counts the boxes containing part of the structure. The number of boxes $N(\varepsilon)$ was evaluated for progressively small box sizes.

From the slope of the linear region in the plot of $\log N(\varepsilon)$ *vs.* $\log(1/\varepsilon)$, the fractal dimension was obtained as: $D = \lim_{\varepsilon \to 0} \log N(\varepsilon)/\log(1/\varepsilon)$. Power spectral density analysis was used to reveal self-similar properties in the frequency domain. Starting from each FE-SEM image, the Fourier transform was computed, and the squared magnitude provided the power at each frequency (f). The plot of $\log P(f)$ *vs.* $\log f$ was obtained, where the slope of the linear region indicated the scaling behavior, *i.e.* $P(f) \propto f^{-\beta}$. Lacunarity analysis was performed by overlaying the image (binary or grayscale) with a sliding box of size r and counting the number of foreground pixels in each box. The lacunarity ($\Lambda(r)$) was calculated as $\Lambda(r) = \text{variance}(r)/[\text{mean}(r)]^2 + 1$. The slope of the $\log \Lambda(r)$ *vs.* $\log r$ plot was evaluated by fitting the curve in a log–log scale. A negative slope indicated decreasing lacunarity with scale, which was consistent with self-similarity. The mean perimeter–area analysis is based on identifying shapes with perimeter P and area A in the FE-SEM images. While in Euclidean geometry (*e.g.* squares) P scales as $A^{1/2}$, for irregular or fractal-like shapes, the perimeter increases faster with area, following $P \propto A^{D/2}$, with $D > 1$. The value of D was obtained from the slope of the log–log plot of P *vs.* A. The results from box-counting and lacunarity are reported in Fig. 2a and b. The complete analysis is reported in the SI file.

Based on all these steps, the fractal analysis indicated that the average fractal dimension obtained *via* box-counting was $D = 2.01$. Furthermore, the mean lacunarity slope was -0.52, indicating a non-random and heterogeneous distribution of voids. The mean perimeter–area exponent, $D = 1.18$, reflected the presence of highly irregular and complex boundaries. Finally, the spectral exponent ($\beta = 3.24$) estimated through the power spectral density analysis corresponded to a Fourier

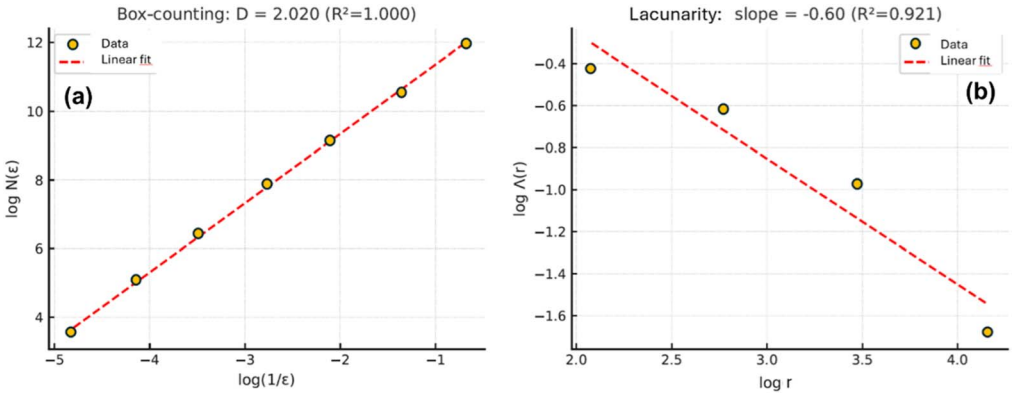

Fig. 2 Box-counting (a) and lacunarity (b) plots obtained from the analysis of the SEM images.

fractal dimension ($D_{(Fourier)} = 2.62$). Taken together, these four independent analyses converged to support the presence of robust fractal characteristics across the 15–500 nm spatial scale.

3.2 XPS spectroscopy

XPS spectroscopy measurements were carried out to investigate the oxidation of the Ni NP layer, as well as to determine changes in the C chemical environment upon the deposition of the NiO overlayer. Core-level Ni 2p XPS data are shown in Fig. 3a. For all samples, Ni turned out to be oxidized to NiO, in agreement with the reference literature[51–53] and recent results on nanostructured NiO.[37,41] Indeed, the binding energy (BE) and the charge-transfer satellite structure in both Ni $2p_{3/2}$ (A, B features) and Ni $2p_{1/2}$ (C and D features) spin–orbit split components are quite similar to those observed in high-quality NiO single-crystals, taken as a reference. Metallic nickel is known to yield a main line at a binding energy of 2.0 eV below the main line of NiO (as reviewed and discussed in ref. 43) and should be visible. This feature was not present in any of our samples. Therefore we rule out the presence of metallic nickel contribution within the sensitivity of the experimental probe, which can be defined as better than 1% atomic on the basis of the instrumental resolution and quality of the XPS data. Core level C 1s XPS spectra are shown in Fig. 3b. All spectra displayed a broad and asymmetric C 1s peak that, in general, can account for different contributions from graphitic C sp^2, C sp^3 and additional defective carbon, as well as oxygen-related contributions at high BEs (C–OH/C–O–C at BE ≈ 286 eV and COOH/COO–R at BE ≈ 288.5 eV).[54] These oxygen-related contributions at high BEs were tentatively ascribed to physisorbed species due to air exposure and oxygen trapped between the graphene layer and the insulating Si_3N_4 layer during the transfer of graphene. When the samples were annealed under ultra-high vacuum conditions, the intensity of these broad peaks was reduced significantly, which was consistent with their main origin as adventitious species adsorbed on the surface.

Finally, the two kinds of possible defects were considered, namely sp^3 carbon at BE = 285.4 eV (ref. 55) and defective carbon at BE = 283.5 eV.[56] The broad structure of the C 1s peak did not allow for an unambiguous detection of the sp^3-related peak. In turn, a comparison between the C 1s peaks measured on pristine graphene and on the S3 sample, which was the best performing layer in terms of chemiresistive sensing (see paragraph 3.4), displayed an evident asymmetry on the low-BE side (marked with a vertical arrow in Fig. 3b). This feature could be ascribed, following Blume *et al.*,[56] to defects in carbon similar to those produced by surface sputtering, and therefore, it is more likely related to carbon vacancies in the Gr lattice.

The detailed fitting of the C 1s XPS spectra is shown in the SI file, where the pristine graphene layer, a vacuum-annealed pristine graphene layer and the S3 layer are considered. The spectral features are labelled according to the review analysis found in ref. 54 and 56.

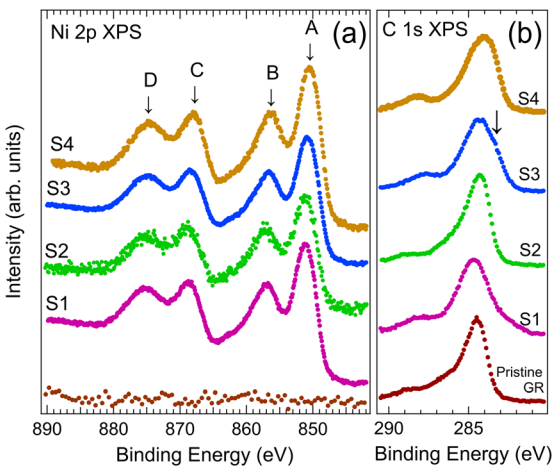

Fig. 3 (a) Ni 2p and (b) C 1s XPS spectra of pristine graphene and the four NiO–GR sensing layers.

3.3 Raman spectroscopy

The microRaman mapping of the different samples was carried out in order to (i) check the sample homogeneity—with a lateral resolution of about 1 μm, provided by the microscope objective coupled to the Raman spectrometer—and (ii) discuss the doping effects. The full-range Raman spectra are shown in Fig. S8 of the SI, where the presence of possible impurities is also discussed in connection with interference effects arising at the Si_3N_4 buffer layer sandwiched between the silicon substrate and the top-most graphene layer (Fig. S9 and S10 of the SI and related discussion).

In the present study, the doping of the sensing layers had a three-fold origin. First of all, the doping resulted from the exposure of the sensing layer to the lab environment. Interaction with moisture in the air is known to induce a p-type doping in graphene.[57] Another source of possible doping arises when the NiO–Gr interface is created. Finally, doping can be induced by gas adsorption. The first two stages were probed by the analysis of the microRaman spectra collected in ambient air. The temporary doping arising from the gas exposure was then determined by the nature of the adsorbing analytes, either NO_2 or NH_3, which are known to be electron acceptors or donors, respectively.[12]

Fig. 4a shows the Raman spectra collected from the 5 samples in the 1550–2750 cm^{-1} wavenumber range, which includes both the G and 2D bands of graphene. In order to evaluate the intensities and wavenumbers for these two bands, we carried out a mapping of sample surfaces, and for each sample, we considered the average of 40 points collected on a square grid, defined to span a few mm^2. With this method, for each sample, the I_{2D}/I_G intensity ratio was also calculated, and the results are shown in Fig. 4b.

The I_{2D}/I_G intensity ratio decreased moving from the pristine sample to those featuring the NiO–Gr interface (Fig. 4b). This was assumed as an indicator of the doping level in the graphene layer.[58] Indeed, the value of the ratio I_{2D}/I_G was larger than 3 for the pristine samples, while it was reduced to a value between 1.2 and 2.5 in the samples with the NiO overlayer. It must also be pointed out that, looking at the I_{2D}/I_G ratio alone, it was not possible to establish whether its shift was due to electron or

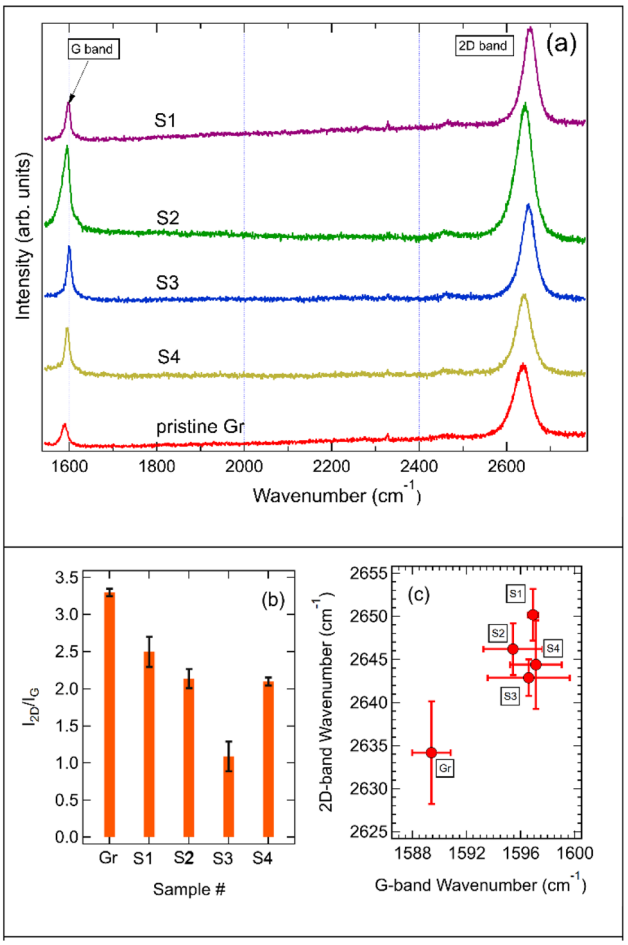

Fig. 4 (a) Representative Raman spectra of the five samples. Gr = pristine graphene. (b) I_{2D}/I_G intensity ratio in pristine graphene (Gr) and in samples with nickel NP deposition (S1–S4). (c) Wavenumber (cm^{-1}) of the G and 2D bands in pristine graphene and in samples with nickel NP deposition.

hole doping, since the behaviour of the ratio was symmetric (it decreased when doping increased, no matter if it was an n-type or p-type doping). Thus, to assess that, we took into account the position of the 2D band, as suggested in ref. 58, which showed that an increase in p-type doping level caused the 2D band to shift to relatively high frequencies, while an increase in the n-type doping level eventually resulted in a 2D-band shift to relatively low frequencies. Based on the present data for the 2D band position (Fig. 4c), we could conclude that the deposition of NiO NPs induced a p-type doping of the graphene layer.

Once the p-type nature of doping was established, by considering the results presented by Das *et al.*[58] on electrochemically doped graphene, the I_{2D}/I_G ratio values presented in Fig. 4b could be compared to those shown in ref. 58 for the hole-branch (Fig. 4 of ref. 58). From this comparison, we could estimate that our S3 layer displayed a hole-doping level of about 2.2×10^{13} cm^{-2}, while all the other samples looked slightly p-doped, with hole concentrations ranging from 0.0 to 0.4×10^{13} cm^{-2}.

3.4 Chemiresistive behavior

A selected example of a dynamical response for sample S3 and the calibration curves for the five sensing layers are shown in Fig. 5 for both NH_3 (Fig. 5a) and NO_2 (Fig. 5c) gas exposures. For each target gas, three exposures were presented at variable concentrations, *i.e.* 17.8, 11.0, and 0.6 ppm for NH_3 and 2.25, 3.0, and 3.5 ppm for NO_2. In all cases, the exposure time was 300 seconds, and a time of about two hours was left for recovery to the baseline resistance (R_0). As could be observed, exposure to NO_2 afforded a decrease in the resistance (Fig. 5c), while exposure to ammonia (Fig. 5a) afforded an increase in resistance. This is the expected behavior of a p-type graphene layer. In the case of NO_2, the calibration curves (Fig. 5d) showed that the NiO–graphene interfaces had a relatively low sensitivity with respect to the pristine layer, while an increase in sensitivity was registered for sample S3 upon exposure to NH_3 (Fig. 5b). Both findings indicated that, at least for the S3 sample, the nanostructured NiO layer made the overall sensing layer more selective to NH_3 by increasing the response to NH_3 and decreasing the response to NO_2. Sample S4 did not show appreciable resistance changes during NO_2 exposure. All calibration curves were fit with a Freundlich isotherm, which is usually considered as a reference isotherm for these chemiresistors.[6,10]

These isotherms appear as dashed lines in Fig. 5b and d. The parameters resulting from the fit are reported in Table S1. The simultaneous behavior of the five sensing layers upon NH_3 exposure is shown in Fig. S3.

In principle, sensing measurements can be affected by batch-to-batch variations and surface stability. In our case, batch-to-batch variation was primarily determined by the features of the pristine layer, since we noted changes in the graphene layer features depending on the production batch, as detailed in Fig. S4. To overcome this issue, we prepared our sensing layers by using samples from the same production

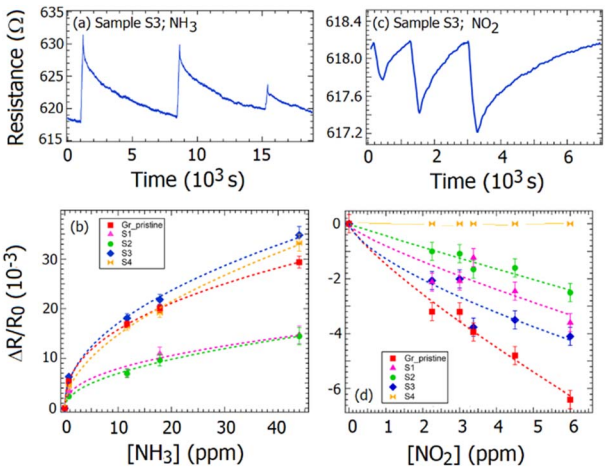

Fig. 5 Chemiresistive dynamical response of the S3 sensor to (a) NH_3 (17.8, 11.0, and 0.6 ppm) and (c) NO_2 (2.25, 3.0, and 3.5 ppm) as target gas molecules. Relative change ($\Delta R/R_0$) in resistance after exposures to NH_3 (b) and NO_2 (d) and *vs.* analyte concentration. Dashed lines: data fitting with the Freundlich isotherms.

batch, avoiding the use of samples purchased at different times. Focusing on the S3 and pristine layers, the data collected about 9 months later (Fig. S5 of the SI) showed that sample S3 still behaved better than the pristine one under NH_3 exposure and worse under NO_2 exposure, confirming the stability of the surface reactivity across time.

It is interesting to point out that the latest measurements, aimed to probe the stability over time, were both carried out in a sealed chamber with a low R.H. content (4%), while those reported in Fig. 5 were carried out in the lab atmosphere at R.H. = 50% for NH_3 and in a sealed chamber at R.H. = 4% for NO_2. As water is recognized as a p-dopant in single layer graphene,[57] the measurements at high R.H. increase p-doping of graphene and therefore the reactivity towards NH_3, consistently with the data reported in Table S2, where response to NH_3 is found to increase with R.H. On the other hand, relatively high R.H. values are representative of ordinary ambient conditions typical of gas sensing environments (for both indoor and outdoor monitoring), suggesting that the present sensing layers can be used in real operating conditions, provided that R.H. is constantly monitored.

As previously discussed, the analysis of the surface morphology showed that the highest amount of NPs was expected for sample S4. The fact that S4 behaved less efficiently with respect to S3 as a chemiresistor could be explained by the assumption that S4 was too thick for an efficient transport of charges from the sensing layer surface to the underneath graphene layer, which also acted as the transport layer.

Comparison with the sensing data and performances of systems based on Gr–NiO sensing layers[28–44] is not straightforward. In fact, most of them deal with rGO, usually presenting composites or systems where NiO NPs decorate graphene rather than being used to produce a heterojunction. Furthermore, only a few of them test sensing layers against both NH_3 and NO_2, and most of the tests are for NO_2. Among all papers, only ref. 31 and 41 can be referenced for benchmarking with our results. The sensitivity to NH_3 in ref. 31 outperforms our results when NiO is used to functionalize graphene. The implementation of GFET, as in the present study, could provide further advancement in sensitivity and selectivity. Ref. 41 describes a layer-stacking scheme very similar to the one we propose. NiO was deposited by MBE on high quality Gr grown on SiC. Sensitivity to NO_2 seems to decrease with NiO, as in our case, but measurements for NH_3 are missing, and selectivity cannot be probed at this stage.

3.5 GFET characterization

GFET measurements were carried out at several NH_3 concentrations, such as 0, 13, 27, 32, 38, and 71 ppm. After stabilizing each NH_3 concentration in the exposure chamber, a quick (10 s) I_{DS} *vs.* V_{GATE} scan (hereinafter reported as *I–V* characteristic) was carried out (Fig. 6a). It could be noticed that the Dirac point upshifted while increasing the NH_3 concentration. Based on these measurements, a calibration curve was extracted (Fig. 6b) considering the shift of the Dirac point induced by the interaction with NH_3 (V_{GATE}) with respect to the gate voltage of the

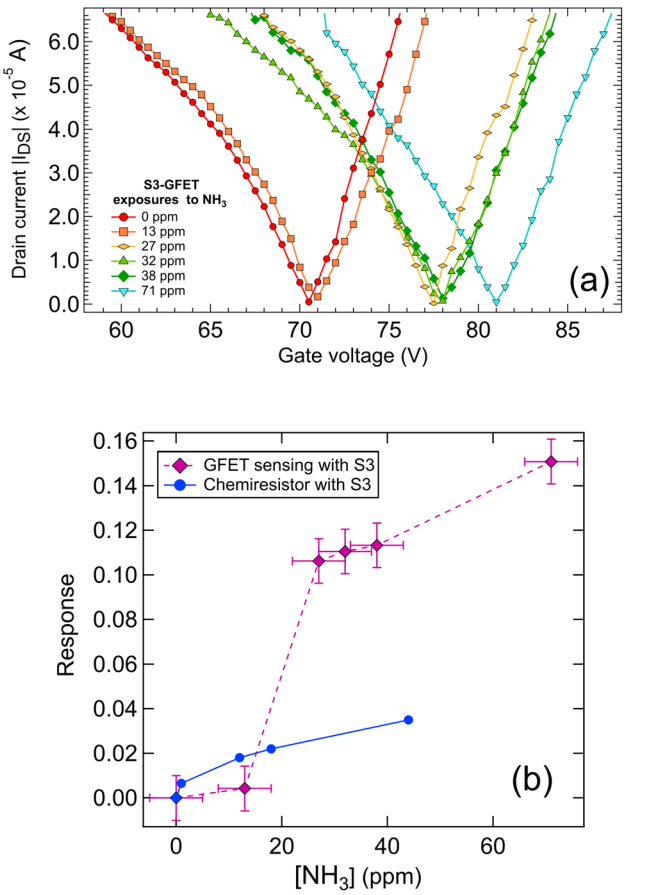

Fig. 6 (a) Example of GFET measurements carried out using the sample S3 as the sensing device. For each concentration, several *I–V* cycles were collected and averaged in order to track the shift in the Dirac point upon changes in the NH_3 concentration. (b) Calibration curves obtained from the GFET measurements carried out using the sample S3 as the sensing device. Zero reference is the measure in ambient air without NH_3. The purple diamonds and the blue circles show the calibration curves obtained from the GFET and chemiresistor, respectively.

Dirac point measured in the absence of gas ($V_{GATE,0}$). With these data, the response, *R*, is defined as $R = \Delta V_{gate}/V_{gate,0}$, with $\Delta V_{gate} = V_{gate} - V_{gate,0}$. The data showed a trend similar to that observed using the devices as chemiresistors. However, the response (*R*) ($\Delta V_{gate}/V_{gate,0}$) for NH_3 above 20 ppm was much larger than the response obtained in the chemiresistive readout ($\Delta R/R_0$). This conclusion proves that the GFET readout scheme can be more effective than the simple chemiresistor readout in the detection of NH_3.

When plotted for a large voltage range, the *I–V* characteristics appeared to be strongly asymmetric for positive and negative bias, as shown in Fig. 7. The observed asymmetry in the *I–V* characteristics of the GFET could be attributed to charge impurity scattering, which induced electron–hole mobility asymmetry in graphene. As demonstrated in previous studies, charged impurities near the graphene channel create spatial fluctuations in the electrostatic potential, leading to localized electron and hole domains and modifying carrier transport

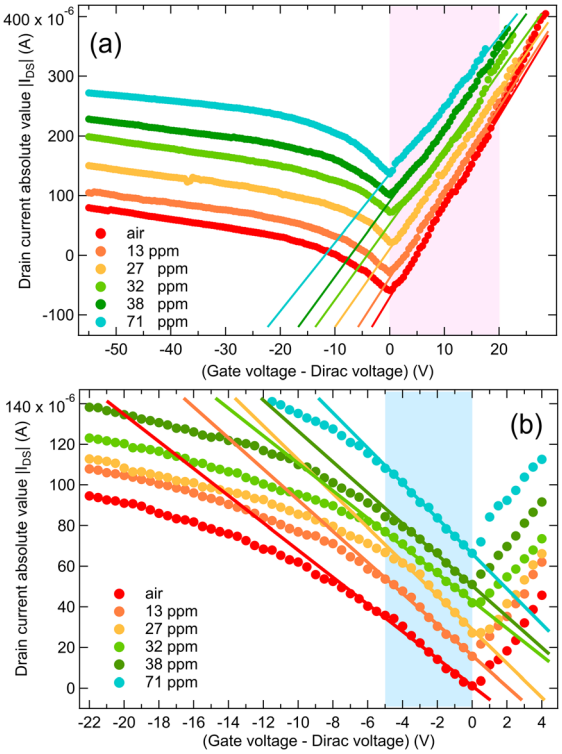

Fig. 7 Linear fitting of the *I*–*V* curves, obtained from the sample S3 upon NH_3 exposure, for carrier mobility estimations. Hole (a) and electron (b) branch fitting. The voltage ranges considered for linear interpolation are highlighted as shaded windows. Curves have been aligned to $V = 0$ by considering, for each curve, the V_{gate}–$V_{Dirac\ point}$ of the original curves and stacked on the vertical axis to better display details of the linear fitting.

properties.[59] Additionally, the presence of short-range scattering centers can further influence the transport asymmetry, particularly in regions of high carrier density.[60] These effects are more pronounced in functionalized or surface-modified graphene, where doping-induced charge inhomogeneities affect the shift in the Dirac point and lead to an imbalance between electron and hole conduction.

Finally, the mobility of carriers was determined from the *I*–*V* curves, with the aim of tracking a possible dependence of mobility on the interaction of NH_3 with the sensing layer. Therefore, both branches of the *I*–*V* curve were fitted with a line in the −20–0 V window, highlighted in pink in Fig. 7a, and in the 0–5 V window (light blue region in Fig. 7b) after all *I*–*V* curves were shifted by setting the Dirac point at 0 V. Following ref. 61–63, from the fitting of the linear part of the *I*–*V* curves, the hole mobility (μ_h), as shown in Fig. 7a, was extracted from the slope, *a*, according to the following formula:

$$a = -V_{SD}\mu_h C_{TOT},$$

where V_{SD} is the source–drain voltage, and C_{TOT} is the total capacity of the device, which is mainly determined by the capacitance of the dielectric layer and by the quantum capacitance of graphene. Further, *a* is the slope of the fitting lines of the hole (electron) branches of the *I*–*V* curve.[64] Similarly, the

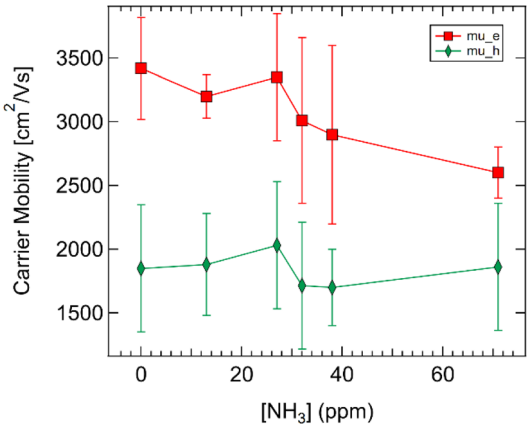

Fig. 8 Mobility of holes (μ_h, diamonds) and electrons (μ_e, squares) *vs.* NH_3 concentration.

electron mobility, μ_e, was extracted from the fitting of the electron branch curves (Fig. 7b), on the basis of the relationship $a = V_{DS}\mu_e C_{TOT}$ between the slope (α) and the electron mobility (μ_e).

The hole and electron mobility values *vs.* the NH_3 concentration are shown in Fig. 8. We registered a decrease in the electron mobility with the NH_3 concentration from about 3500 $cm^2\ V^{-1}\ s^{-1}$ to 2600 $cm^2\ V^{-1}\ s^{-1}$. In turn, the hole mobility fluctuated around 1800 $cm^2\ V^{-1}\ s^{-1}$, as the NH_3 concentration increased from 0 to 71 ppm.

The mobility trends can be linked to charge impurity scattering effects.[65] The asymmetry in electron and hole mobilities was indicative of the influence of donor and acceptor impurities, which affected carrier transport differently due to their attraction-repulsion asymmetry in scattering cross-sections. The reduction of μ_e with increasing NH_3 concentration suggested that Coulomb scattering dominated the transport properties, with mobility scaling inversely with impurity density. This behavior was consistent with prior theoretical predictions describing that charge inhomogeneities strongly impacted carrier mobility in graphene-based devices.[65]

4 Conclusions

An interface between graphene and a nanostructured, fractal-like NiO layer was prepared by a dry printing process based on spark ablation. XPS data indicated that NiO NPs resulted from the full oxidation of Ni when these NPs stuck onto the graphene layer. Consistent with the Raman data, transport measurements (chemiresistor and GFET) indicated that the effect of the nanostructured NiO layer was to strengthen the p-type character on the best-performing sensing layer, thereby increasing the selectivity towards NH_3 detection. With respect to the pristine graphene layer, the response to NO_2 decreased by a factor of approximately 2 over the NO_2 concentration range from 2 to 6 ppm, while we registered a 3-fold increase in the response to NH_3 over a concentration range of 10–40 ppm. Finally, the GFET architecture further increased the sensitivity to NH_3 with respect to the chemiresistive readout of about 3

times, thereby providing a strategy that could be generalized to improve the selectivity to specific analytes by switching from a simple chemiresistor to a GFET readout scheme.

Author contributions

M. Z.: investigation, writing – review & editing, data curation, validation; E. R.: investigation, writing – review & editing; S. F.: investigation, writing – review & editing; S. P.: writing – review & editing, validation; V. M. writing – review & editing, resources; F. R.: resources, investigation, writing – review & editing; Le. S.: resources, investigation, writing – review & editing; Lu. S.: resources, validation, visualization, writing – original draft.

Conflicts of interest

There are no conflicts to declare.

Data availability

The data supporting this article have been included partially in the supplementary information (SI) and are available upon request to the authors. Supplementary information: optical and SEM microscopy analysis. Dynamical response to NH_3 from all samples. Response to NO_2 and NH_3 after 9 months. Batch-to-batch variation. Calibration curves after 9 months. FE-SEM image analysis for fractal dimension estimation. Additional Raman spectroscopy data. Analysis of interference effects due to the Si_3N_4 buffer layer. XPS analysis and fitting of selected C 1s core level data. See DOI: https://doi.org/10.1039/d5ra06573a.

Acknowledgements

M. Z. acknowledges support from the School of Doctorate in Science under the joint PhD program, UNICATT-KU Leuven. S. F. acknowledges Fondazione Cariplo, within the grant BREATH-SENSE 2023-1506 – 'Giovani Ricercatori 2023' call.

Notes and references

1 R. A. Bueno, J. I. Martínez, R. F. Luccas, N. Ruiz del Árbol, C. Munuera, I. Palacio, F. J. Palomares, K. Lauwaet, S. Thakur, J. M. Baranowski, W. Strupinski, M. F. López, F. Mompean, M. García-Hernández and J. A. Martín-Gago, *Nat. Commun.*, 2017, **8**, 15306.
2 G. Ambrosio, A. Brown, L. Daukiya, G. Drera, L. Di Santo, G. Petaccia, S. De Feyter, L. Sangaletti and S. Pagliara, *Nanoscale*, 2020, **12**, 9032.
3 V. Georgakilas, J. N. Tiwari, K. C. Kemp, J. A. Perman, A. B. Bourlinos, K. S. Kim and R. Zboril, *Chem. Rev.*, 2016, **116**, 5464.
4 J. Li, P. Brandimarte, M. Vilas-Varela, N. Merino-Díez, C. Moreno, A. Mugarza, J. S. Mollejo, D. Sánchez-Portal, D. Garcia De Oteyza, M. Corso, A. Garcia-Lekue, D. Peña and J. I. Pascual, *ACS Nano*, 2020, **14**, 1895.
5 B. Cho, J. Yoonb, M. G. Hahma and D. H. Kim, *J. Mater. Chem. C*, 2014, **2**, 5280.
6 B. Alfano, T. Polichetti, M. Mauriello, M. L. Miglietta, F. Ricciardella, E. Massera and G. Di Francia, *Sens. Actuators, B*, 2016, **222**, 1032.
7 S. Freddi, M. C. R. Gonzalez, P. Carro, L. Sangaletti and S. De Feyter, *Angew. Chem., Int. Ed.*, 2022, **61**, e202200115.
8 B. H. Chu, C. Lo, J. Nicolosia, C. Chang, V. Chen, W. Strupinski, S. J. Pearton and F. Ren, *Sens. Actuators, B*, 2011, **157**, 500.
9 F. Ricciardella, S. Vollebregt, T. Polichetti, M. Miscuglio, B. Alfano, M. L. Miglietta, E. Massera, G. Di Francia and P. M. Sarro, *Nanoscale*, 2017, **9**, 6085.
10 D. Perilli, S. Freddi, M. Zanotti, G. Drera, A. Casotto, S. Pagliara, L. Schio, L. Sangaletti and C. Di Valentin, *Commun. Mater.*, 2024, **5**, 254.
11 A. Paghi, S. Mariani and G. Barillaro, *Small*, 2023, **19**, 2206100.
12 F. Schedin, A. K. Geim, S. V. Morozov, E. W. Hill, P. Blake, M. I. Katsnelson and K. S. Novoselov, *Nat. Mater.*, 2007, **6**, 652.
13 X. Yan, Y. Wu, R. Li, C. Shi, R. Moro, Y. Ma and L. Ma, *ACS Omega*, 2019, **4**, 14179.
14 T. Ikuta, T. Tamaki, H. Masai, R. Nakanishi, K. Endo, J. Terao and K. Maehashi, *Nanoscale Adv.*, 2021, **3**, 5793.
15 G. Lu, L. E. Ocola and J. Chen, *Appl. Phys. Lett.*, 2009, **94**, 8.
16 M. Gautam and A. H. Jayatissa, *J. Appl. Phys.*, 2012, **112**, 064304.
17 P. L. Levesque, S. S. Sabri, C. M. Aguirre, J. Guillemette, M. Siaj, P. Desjardins, T. Szkopek and R. Martel, *Nano Lett.*, 2011, **11**, 132.
18 B. Kumar, K. Min, M. Bashirzadeh, A. Barati Farimani, M.-H. Bae, D. Estrada, Y. D. Kim, P. Yasaei, Y. D. Park, E. Pop, N. R. Aluru and A. Salehi-Khojin, *Nano Lett.*, 2013, **13**, 1962.
19 Y. Liu, H. Liu, Y. Chu, Y. Cui, T. Hayasaka, V. Dasaka, L. Nguyen and L. Lin, *Adv. Mater. Interfaces*, 2018, **5**, 1701640.
20 S. Masoumi and H. Hajghassem, *Sens. Rev.*, 2019, **39**, 819.
21 H. Vedala, D. C. Sorescu, G. P. Kotchey and A. Star, *Nano Lett.*, 2011, **11**, 2342.
22 M. Zanotti, S. Freddi and L. Sangaletti, *Adv. Mater. Technol.*, 2025, **10**, 2400985.
23 A. Milone, A. G. Monteduro, S. Rizzato, A. Leo, C. Di Natale, S. S. Kim and G. Maruccio, *Adv. Sustainable Syst.*, 2023, **7**, 2200083.
24 M. Galvani, S. Freddi and L. Sangaletti, *Sensors*, 2024, **24**, 584.
25 N. Norhakim, T. Gunasilan, Z. Rafi Kesuma, H. Fahmi Hawari and Z. Arif Burhanudin, *Nanotechnology*, 2024, **35**, 505201.
26 C. Loizidis, K. C. Petallidou, A. Maisser, S. Bezantakos, T. V. Pfeiffer, A. Schmidt-Ott and G. Biskos, *Aerosol Sci. Technol.*, 2024, **58**, 1421.
27 L. N. Sacco, N. Schouten; L. Egger, M. Popov, A. Köck, C. Dösinger and L. Romaner, *2024 IEEE Sensors Conference*, 2024, p. 7101, DOI: 10.1109/SENSORS60989.2024.10785068.
28 D. Sun, Y. Luo, M. Debliquy and C. Zhang, *Beilstein J. Nanotechnol.*, 2018, **9**, 2832.

29 C. Walleni, M. Ben Ali, M. Faouzi Ncib and E. Llobet, *Sensors*, 2025, **25**, 1631.
30 T. Kamal, *J. Alloys Compd.*, 2017, **729**, 1058.
31 S. Kim, Y. Kim, J. Kim, S. J. Kim, T. Kim, J. Sim, S. E. Jun, J. Lim, T. Hoon Eom, H. S. Lee, G.-H. Lee, B. H. Hong, M.-H. Oh, Y. S. Huh and H. W. Jang, *Adv. Funct. Mater.*, 2024, **34**, 2407885.
32 J. Zhang, D. Zeng, S. Zhao, J. Wu, K. Xu, Q. Zhu, G. Zhang and C. Xiea, *Phys. Chem. Chem. Phys.*, 2015, **17**, 14903.
33 J. Zhang and D. Zeng, *2014 IEEE Sensors Conference*, 2014, p. 277, DOI: 10.1109/ICSENS.2014.6984987.
34 C. A. Zito, T. M. Perfecto, C. S. Fonseca and D. P. Volanti, *New J. Chem.*, 2018, **42**, 8638.
35 F. D. Matthe, O. M. Nwakanma, A. C. Nkele, A. Alshoaibi, S. U. Offiah, P. K. Alor, G. H. Jain, S. D. Shinde, B. A. Ezekoye, A. B. C. Ekwealor, G. E. Patil and F. I. Ezema, *J. Mater. Res.*, 2025, **40**, 1034–1045.
36 F. Mehmood, S. Siddique, A. Shakoor, J. Hussain, G. Naz, S. A. Shah and M. Arshad, *Eng. Res. Express*, 2025, **7**, 025010.
37 N. Thakur, H. Murthy, S. Arumugam, N. Thomas, A. M. Koshy and P. Swaminathan, *J. Semicond.*, 2025, **46**, 012606.
38 A. C. Nkele, A. Alshoaibi, F. D. Matthew, C. Awada, S. Islam and F. J. Ezema, *J. Sol-Gel Sci. Technol.*, 2025, **114**(3), 874–884.
39 M. D. Femi, A. C. Nkele, M. O. Nwakanma, A. Alshoaibi, G. H. Jain, S. D. Shinde, B. A. Ezekoye, A. B. C. Ekwealor, S. M. Abhinay, G. E. Patil and F. I. Ezema, *J. Sol-Gel Sci. Technol.*, 2025, **114**, 326–337.
40 S. Alotaibi, A. M. Bakry, S. Hassaballa, K. S. Amin and H. Elhaes, *Phys. Scr.*, 2025, **100**(10), 105942.
41 S. S. Niavol, M. Budde, A. Papadogianni, M. Heilmann, H. Milani Moghaddam, C. M. Aldao, G. Ligorio, E. J. W. List-Kratochvil, J. M. J. Lopes, N. Barsan, O. Bierwagen and F. Schipani, *Sens. Actuators, B*, 2020, **325**, 128797.
42 M. Yang, L. Liu, B. Li, Y. Xu and L. Huo, *Appl. Surf. Sci.*, 2026, **720**, 165191.
43 M. Ben Arbia and E. Comini, *Chemosensors*, 2024, **12**, 45.
44 T. S. Balaji, S. Balaji, P. Rathinakumar and S. Karthik, *Chem. Phys. Impact*, 2026, **12**, 100992.
45 M. Chiesa, F. Rigoni, M. Paderno, P. Borghetti, G. Gagliotti, M. Bertoni, A. Ballarin Denti, L. Schiavina, A. Goldoni and L. Sangaletti, *J. Environ. Monit.*, 2012, **14**, 1565.
46 S. Freddi, A. V. Emelianov, I. I. Bobrinetskiy, G. Drera, S. Pagliara, D. S. Kopylova, M. Chiesa, G. Santini, N. Mores, U. Moscato, A. G. Nasibulin, P. Montuschi and L. Sangaletti, *Adv. Healthcare Mater.*, 2020, **9**, 2000377.
47 M. Li, C. J. Weschler, G. Bekö, P. Wargocki, G. Lucic and J. Williams, *Environ. Sci. Technol.*, 2020, **54**, 5419.
48 N. T. Brannelly, J. P. Hamilton-Shield and A. J. Killard, *Crit. Rev. Anal. Chem.*, 2016, **46**, 490.
49 W. Zhang, D.-W. Sun, J. Ma, Z. Wang, A. Qin and B. Z. Tang, *Food Chem.*, 2023, **418**, 135929.
50 G. Drera, G. Salvinelli, J. Åhlund, P. G. Karlsson, B. Wannberg, E. Magnano, S. Nappini and L. Sangaletti, *J. Electron Spectrosc. Relat. Phenom.*, 2014, **195**, 109.
51 L. Sangaletti, L. E. Depero and F. Parmigiani, *Solid State Commun.*, 1997, **103**, 421.
52 A. P. Grosvenor, M. C. Biesinger, R. S. Smart and N. S. McIntyre, *Surf. Sci.*, 2006, **600**, 1771.
53 F. Parmigiani and L. Sangaletti, *J. Electron Spectrosc. Relat. Phenom.*, 1999, **98**, 287.
54 X. Chen, X. Wang and D. Fang, *Fullerenes, Nanotubes Carbon Nanostruct.*, 2020, **28**, 1048.
55 G. Ambrosio, G. Drera, G. Di Santo, L. Petaccia, l. Daukiya, A. Brown, B. Hirsch, S. De Feyter, L. Sangaletti and S. Pagliara, *Sci. Rep.*, 2020, **10**, 4114.
56 R. Blume, D. Rosenthal, J.-P. Tessonnier, H. Li, A. Knop-Gericke and R. Schlogl, *ChemCatChem*, 2015, **7**, 2871.
57 C. Melios, A. Centeno, A. Zurutuza, V. Panchal, C. E. Giusca, S. Spencer, S. R. P. Silva and O. Kazakova, *Carbon*, 2016, **103**, 273.
58 A. Das, S. Pisana and B. Chakraborty, *Nat. Nanotechnol.*, 2008, **3**, 210.
59 J.-H. Chen, C. Jang, S. Adam, M. S. Fuhrer, E. D. Williams and M. Ishigami, *Nat. Phys.*, 2008, **4**, 377.
60 J. H. Gosling, O. Makarovsky, F. Wang, N. D. Cottam, M. T. Greenaway, A. Patanè, R. D. Wildman, C. J. Tuck, L. Turyanska and T. M. Fromhold, *Commun. Phys.*, 2021, **4**, 30.
61 D. Jimenez, *IEEE Trans. Electron Devices*, 2011, **58**, 4377.
62 S. A. Thiele, J. A. Schaefer and F. Schwierz, *J. Appl. Phys.*, 2010, **107**, 094505.
63 M. Bonmann, A. Vorobiev, J. Stake and O. Engström, *J. Vac. Sci. Technol., B*, 2017, **35**, 01A115.
64 T. Fang, A. Konar, H. Xing and D. Jena, *Appl. Phys. Lett.*, 2007, **91**, 092109.
65 D. S. Novikov, *Appl. Phys. Lett.*, 2007, **91**, 102102.